Danny Bottenus
Talukder Zaki Jubery*
Prashanta Dutta*
Cornelius F. Ivory

Gene and Linda Voiland School of Chemical Engineering and Bioengineering, Washington State University, Pullman, WA, USA

Received September 30, 2010
Revised December 2, 2010
Accepted December 5, 2010

Research Article

10 000-fold concentration increase in proteins in a cascade microchip using anionic ITP by a 3-D numerical simulation with experimental results

This paper describes both the experimental application and 3-D numerical simulation of isotachophoresis (ITP) in a 3.2 cm long ''cascade'' poly(methyl methacrylate) (PMMA) microfluidic chip. The microchip includes 10 × reductions in both the width and depth of the microchannel, which decreases the overall cross-sectional area by a factor of 100 between the inlet (cathode) and outlet (anode). A 3-D numerical simulation of ITP is outlined and is a first example of an ITP simulation in three dimensions. The 3-D numerical simulation uses COMSOL Multiphysics v4.0a to concentrate two generic proteins and monitor protein migration through the microchannel. In performing an ITP simulation on this microchip platform, we observe an increase in concentration by over a factor of more than 10 000 due to the combination of ITP stacking and the reduction in cross-sectional area. Two fluorescent proteins, green fluorescent protein and *R*-phycoerythrin, were used to experimentally visualize ITP through the fabricated microfluidic chip. The initial concentration of each protein in the sample was 1.995 μg/mL and, after preconcentration by ITP, the final concentrations of the two fluorescent proteins were 32.57 ± 3.63 and 22.81 ± 4.61 mg/mL, respectively. Thus, experimentally the two fluorescent proteins were concentrated by over a factor of 10 000 and show good qualitative agreement with our simulation results.

Keywords:
3-D numerical simulation / Cascade microfluidic chip / Isotachophoresis / Preconcentration / Proteins
DOI 10.1002/elps.201000510

1 Introduction

Preconcentration of biomolecules is a crucial step in the detection of low-abundance molecules [1]. This is especially true in the detection of Iow-abundance molecules of interest where the concentration of the original solution exceeds the detection limits of the instrumentation [2]. Preconcentration is even more important when analyzing complex samples such as blood, spinal fluid, cerebrospinal fluid, saliva, etc., where the sample volume is limited and the amount of material one is trying to detect is small. In the last decade, microfluidic techniques have advanced to a point where detection of low-abundance species by preconcentration techniques is readily achievable.

Many preconcentration techniques exist in microfluidics, such as concentration on a membrane [1, 3–5], solid-phase extraction [6], electrochromatography [7], solid-phase extraction using monoliths [8, 9], sample stacking [10–12], microchip electrophoresis-based immunoassays [13], isoelectric focusing (IEF) [14], and isotachophoresis (ITP) [15–19]. All these techniques have their advantages and limitations. However, the simplest preconcentration technique to implement in microfluidics may be ITP, which has the ability to preconcentrate by several orders of magnitude [17, 20, 21].

ITP is a common electrophoresis technique dating back to the 1970s which is used to analyze charged analytes such

Correspondence: Dr. Cornelius F. Ivory, Gene and Linda Voiland School of Chemical Engineering and Bioengineering, Washington State University P.O. Box 642710, Pullman, WA 99164-2710, USA
E-mail: ivory@wsu.edu
Fax: +1-509-335-4806

Abbreviations: EACA, ε-amino-*n*-caproic acid; **GFP,** green fluorescent protein; **LE,** leading electrolyte; **PE,** phycoerythrin; **TE,** trailing electrolyte

*Current address: School of Mechanical and Materials Engineering, Washington State University, Pullman, WA 99163, USA

Colour Online: See the article online to view Figs. 1-7 in colour

as proteins [22–25]. ITP concentrates and fractionates proteins or other charged ions according to electrophoretic mobility (μ_i). ITP is a non-linear process that forms pure zones of each analyte species. The sample is sandwiched between discontinuous buffers, a leading electrolyte (LE) which has a higher effective electrophoretic mobility and a trailing electrolyte (TE) which has a lower effective electrophoretic mobility compared to sample ions.

Santiago and co-workers [17] demonstrated million-fold preconcentration of dye molecules using sample stacking and ITP in a simple T-chip. Mohamadi and co-workers [13] combined ITP with non-denaturing gel electrophoresis to separate labeled human serum albumin from its immunocomplex and concentrated the sample 800-fold. In a more recent paper from the same group [19], a concentration increase of over 2000-fold was obtained for labeled bovine serum albumin and its immunocomplex by optimizing the leading and TEs and using a combination of ITP and microchip gel electrophoresis techniques. In addition, the authors found that a 20 000-fold increase in concentration could be obtained when using a combination of sample stacking, ITP, and microchip gel electrophoresis [19]. The disadvantage of sample stacking is that the conductivity of the sample must be significantly lower (usually 10 × lower) than the conductivity of the LE that limits potential applications, such as working with blood and other highly conductive samples. The work presented here uses only ITP, with no sample stacking, to concentrate fluorescent proteins 10 000-fold in a microfluidic chip that includes two 10 × reductions in cross-sectional area.

Dolnik et al. [26] first demonstrated how trace, low-molecular-weight analytes could be concentrated by performing ITP in tapered microfluidic capillaries. This cascade required multiple LE chambers, valves, and electrodes. Each tapered portion of the channel required cylindrical valves to connect different cross-sectional area channels to each other. In addition, simulation work was performed by Slais [27] describing ITP in tapered capillaries, but no experimental results were included. With advances in microchip fabrication, complex structures have been designed including cross-sectional area changes without the need for valves or multiple chambers. This paper demonstrates another approach to preconcentrate low-abundant proteins using ITP. To the authors' knowledge, performing ITP on proteins in a poly(-methyl methacrylate) (PMMA) microchip with reductions in cross-sectional area has never been demonstrated.

The PMMA-tapered ITP microchip design is shown in Fig. 1. The device is designed with a 100 × reduction from a large cross-sectional area channel (1 mm wide × 100 μm deep × 10 mm long) to a medium cross-sectional area channel (1 mm wide × 10 μm deep × 3 mm long) to a small cross-sectional area channel (100 μm wide × 10 μm deep × 17 mm long). The transition length between the two cross-sectional area changes is 1 mm so that the total length of the channel is 3.2 cm. The reservoirs are approximately 2.5 mm in diameter. The microfluidic chip includes a T-channel to control the mass load of sample (Fig. 1).

A mass balance on the sample indicates that a decrease in cross-sectional area is directly proportional to an increase in concentration, assuming that the width of the band does not change until the concentration reaches its maximum allowable concentration defined by the plateau concentration (see Eq. 2). This is shown below

$$c_i = \frac{M_i}{w_i A} \tag{1}$$

where c_i is the concentration of sample component, M_i is the total mass or molar load of species i, w_i is the peak width of species i, and A is the cross-sectional area of the channel. The cascaded microchannel includes a 100 × reduction in A which will result in a 100 × increase in c_i according to Eq. (1) as long as it does not reach its plateau concentration. At the point where the concentration reaches its plateau concentration, the concentration no longer increases in proportion to the reduction in A. Instead, w will increase with decreasing A. The plateau concentration (c_S) is the maximum allowable concentration in ITP and may be derived from the Kohlrausch regulating function [28] as

$$c_S = c_{LE}\frac{\mu_S(\mu_{LE} - \mu_C)z_{LE}}{\mu_{LE}(\mu_S - \mu_C)z_S} \tag{2}$$

where c_{LE} is the concentration of the LE, μ_s, μ_{LE}, and μ_C are the electrophoretic mobilities of the LE, sample, and counterion, respectively, and z_{LE} and z_S are the charges on the LE and sample, respectively.

Equation (2) indicates that the plateau concentration of any sample component is proportional to the concentration of the LE and a function of the electrophoretic mobilities and charge states of the LE, sample, and counterion and is independent of the electrical field. In the ideal case, no matter how low the initial sample concentration, the sample can, in principle, be concentrated to its plateau concentration [19]. At the plateau concentration, the resulting peaks of ITP stack into square zones rather than the more common Gaussian peaks. This has been demonstrated extensively in ITP simulations [29, 30].

There is a plethora of ITP simulations dating back to the 1980s with the founding work of Bier et al. [31] to describe various electrophoretic separation processes including moving boundary electrophoresis, zone electrophoresis, IEF, and ITP. For the purposes here, only a few ITP simulations will be described. However, for a more comprehensive list, see the recent review published by Thormann et al. [32]. Saville and Palunsinski [33, 34] developed the simulation software GENTRANS to describe electrophoresis transport processes. Mosher et al. [29] came out with ''Dynamics of Electrophoresis,'' the landmark book, summarizing electrophoresis and simulating electrophoresis techniques including ITP. In addition, ITP simulation software is currently available over the Internet including SIMUL 5 [35] available at http://web.natur.cuni.cz/gas to simulate 1-D electrophoresis systems. However, new features of the extended SIMUL 5 software allow users to alter the continuity equations to include variations in the physical space dimensions to

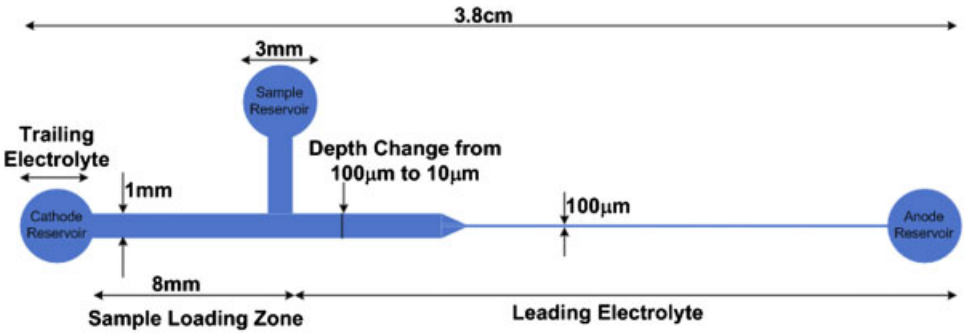

Figure 1. PMMA microchip geometry showing two reducing unions. The total channel length is 3.2 cm with 3 mm id reservoirs. The channel dimensions vary from 1 mm wide and 100 μm deep to 1 mm wide and 10 μm deep to 100 μm wide and 10 μm deep. As the protein sample migrates through different cross-sectional area portions of the channel, the concentration will increase according to Eq. (1). The depth change begins 1 cm from the cathode reservoir and the width change begins 1.3 cm from the cathode reservoir. Each cross-sectional area change occurs over a distance of approximately 1 mm. The microchip includes a T-junction between the sample reservoir and the cathode reservoir in order to control the initial mass load of sample components. Platinum electrodes are inserted into the cathode and anode reservoirs.

incorporate changes in length, diameter, or cross-sectional area in order to perform 2-D simulations [36]. In addition, Santiago and co-workers have developed a MATLAB-based (The MathWorks, Natick, MA) simulation package SPRESSO [37, 38] to describe 1-D ITP which is available online at http://microfluidics.stanford.edu/spresso.

The aforementioned simulation packages have mostly been used as 1-D numerical solvers that give an accurate representation of how ITP and other electrophoretic techniques work in simple systems. However, because of the 1-D nature of these simulation packages, they may not be appropriate for use in all applications and geometries, especially in 3-D. Thus, more sophisticated ITP simulation software is needed to take into account multiple spatial dimensions since ITP is no longer performed only in straight channels or straight capillaries but now in more complex geometries such as constrictions, expansions, and serpentine channels. 2-D numerical simulations of electrophoresis applications are beginning to emerge which describe electrophoretic migration in complex geometries. Shim et al. [39, 40] developed an IEF simulation to describe dispersion of protein bands in a horseshoe microchannel and an IEF simulation that describes protein migration in contraction–expansion microchannels. In addition, there have been recent attempts to simulate IEF in contraction/expansion microchannels by manipulating the conservation equation to include changes in cross-sectional area [41] with results consistent to Shim et al. [39].

In particular, for ITP, Paschkewitz et al. [42] demonstrated 2-D simulations of ITP around a curve using a commercial 2-D finite volume method solver, CFD-ACE (ESI, Huntsville, AL). Cui and co-workers [16] simulated ITP dispersion as proteins migrate past a T-junction in 2-D using a commercially available finite element solver, COMSOL Multiphysics (COMSOL, Burlington, MA). The work presented here presents a 3-D numerical simulation of anionic ITP at high pH values using COMSOL Multiphysics v4.0a and compares these simulation results to experimental results. COMSOL Multiphysics is easy to use and can include the effects of complex geometries such as curves, expansions, and constrictions in three-dimensions. To our knowledge, 3-D numerical ITP simulations have not been reported and are necessary to describe the transport of proteins in complex geometries such as the microfluidic chip (Fig. 1) used in this work.

This work describes ITP in a cascade microchip. The microchip includes two 10× reducing sections so that the concentration of each protein will increase by a factor of 100 according to Eq. (1) plus the ITP concentrating effect, under the assumption that the plateau concentration is not reached prior to the reducing unions. An ITP simulation of a generic protein with initial concentrations of 2.5×10^{-4} mM was concentrated by over a factor of 10 000 using the simulation software COMSOL Multiphysics v4.0a. In addition, ITP experiments were performed on two fluorescent proteins, to monitor protein migration through the microchannel using laser-induced fluorescence detection, and to compare simulation findings with experimental results. The experimental results also demonstrate a concentration factor that exceeds 10 000.

2 Materials and methods

2.1 Materials

Recombinant green fluorescent protein (GFP, MW = 27 000 Da) was purchased from Upstate Biotechnology (Lake Placid, NY, USA). *R*-phycoerythrin (PE, MW = 240 000 Da) was purchased from Molecular Probes (Eugene, OR, USA). GFP and PE are naturally fluorescent proteins under UV excitation. Ethanolamine, ε-amino-*n*-caproic acid (EACA), and polyvinylpyrrolidone K-90 (PVP, MW = 360 000 Da) were purchased from Sigma-Aldrich (St. Louis, MO, USA). Hydrochloric acid (HCl) was purchased from Fisher Scientific (Fair Lawn, NJ, USA).

2.2 LE and TE solutions

The LE solution was prepared by adjusting the pH of 20 mM HCl to pH 9.5 with ≥99% ethanolamine solution. The TE solution consisted of 60 mM EACA titrated to pH 10.0 with ethanolamine. PE and GFP stock solutions were diluted in LE solution to a concentration of 1.995 μg/mL. All the solutions were prepared using nanopure water from a Barnstead Thermolyne Nanopure Infinity UV/UF system (Dubuque, IA, USA) and contained 1% w/v PVP to suppress electroosmotic flow [43]. All solutions were degassed with a CPS-8B vacuum pump (US Vacuum Pumps LLC, Canton, TX, USA) to remove any dissolved gases that can be detrimental to ITP experiments [44].

2.3 Fabrication of microfluidic chip

PMMA is a hard plastic that is an attractive alternative to glass microchips, because PMMA chips can be mass produced rapidly using technologies such as injection molding or hot embossing. PMMA microchips could potentially be used once and then discarded, thus eliminating the serious problems that may arise from cross-contamination and sample carryover for multiple use devices [45]. In addition, PMMA's advantages include excellent optical transparency, biocompatibility, low fluorescence background, and low cost [46]. The PMMA microchip used in this study is formed using a hot embossing technique and a surface modification-assisted bonding method [47]. The detailed fabrication steps are described below and illustrated in Fig. 2.

A positive pattern of the desired channel structure was formed on a glass substrate using negative photolithography (Figs. 2(A–G)). During photolithography, we used multilayer spinning to produce three different depth sections: 100, 10 μm, and a 100–10 μm transition section on our microfluidic chip. For multilayer spinning, a 75 mm × 25 mm × 1 mm glass substrate (Fisher Scientific, PA) was rinsed and cleaned with nanopure water (Fig. 2(A)). Next, ultra-thin PDMS layers were formed using a soft lithography technique [48], trimmed to desired size, and placed on the glass substrate at the desired location (Fig. 2(B)). Then, SU8 2025 (Microchem, MA) was spin-coated (P-6000 Spin Coater, IN) onto the open portion of the glass substrate at 500 rpm for 10 s and at 900 rpm for 30 s. This process yielded a 90 μm thick SU8 layer on the open portion of the glass substrate (Fig. 2(C)). The thin PDMS layer was removed allowing a small amount of SU8 to spread ~1 mm over the previously open portion (Fig. 2(D)). This spread region worked as a transition region between the two different depths of the channel. Next, the SU8 photoresist-coated glass substrate was baked on a hotplate for 5 min at 70°C and in an oven (Thelco, Model19, Precision Scientific, IL) at 95°C for 60 min. SU8 3010 (Microchem) was then spin-coated on the entire glass substrate (at 3000 rpm) including the 90 μm thick SU8 layer to form another 10 μm thick layer on the existing mold (Fig. 2(E)). The SU8 photoresist was baked on a hot plate at 65°C for 5 min and in an oven at 95°C for 60 min. This was followed by placing a patterning mask, which contained the desired image of the microchannel, on the photoresist with alignment to the appropriate depth sections. The photoresist was exposed to near UV light (365 nm) for 2 min using a mask aligner (Hybralign, Series 500, Optical Associates, CA) (Fig. 2(F)). The UV radiation causes the negative resist to become polymerized. Next, the photoresist was baked at 70°C for 3 min on a hotplate, at 100°C for 10 min in an oven, and at 70°C for 5 min on a hotplate. Finally, the photoresist was developed with a commercially available SU8 developer (Microchem) (Fig. 2(G)). The developer solution removed only the unexposed portions of the photoresist, and the negative resist remained on the glass substrate wherever it was exposed. These processes created the desired positive pattern of the microchannel. Finally, the pattern was hard baked at 250°C for 15 min on a hotplate to enhance the cross-linking of the developed SU8 pattern.

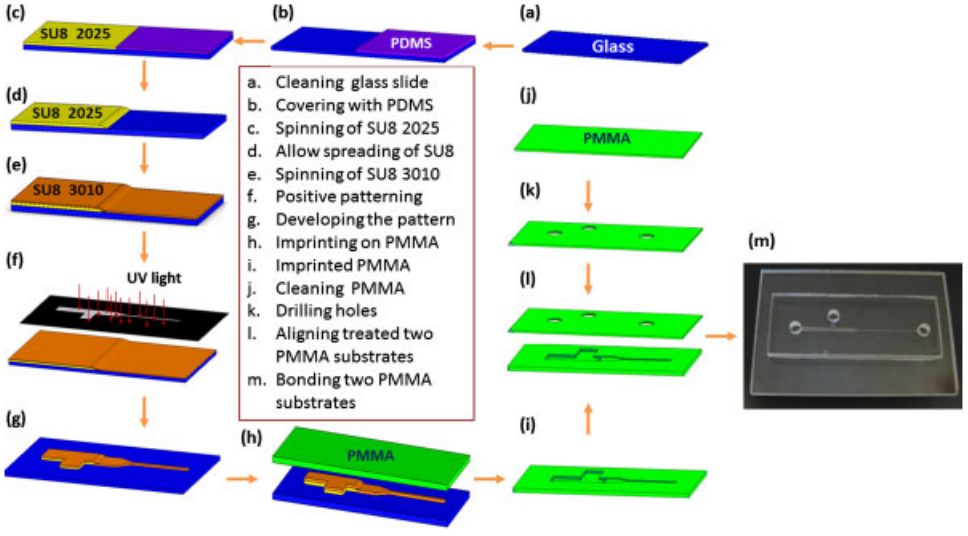

Figure 2. Schematic view of microfabrication techniques to develop step reducing microfluidic chip.

In the next step, the SU8 pattern was hot embossed into a PMMA substrate using a hot press (Fred S. Carver, Summit, NJ). First, a UV transparent PMMA piece (ACRYLITE® OP-4, Evonik Cyro LLC, NJ, USA) was trimmed to size (60 cm × 45 cm × 0.3 cm) and cleaned with soapy water, rinsed, and dried under nitrogen. The glass slide containing the SU8 pattern was placed on a silicon wafer and the PMMA substrate was placed on the SU8 pattern (Fig. 2(H)). The whole assembly was placed on a hot press for 1 min at 120°C. This procedure softens only the surface of the PMMA substrate that was in contact with the SU8 pattern. Then, 200 psi pressure was applied gradually and held at a constant pressure for 1 min. Next, the hot plate was cooled down to room temperature using a built-in water-cooling mechanism. This gradual cooling process reduces the thermal stress and ensures a crack-free microchannel structure. The glass slide was then removed from the PMMA substrate to obtain the bottom layer of the microchip (Fig. 2(I)).

Our next step was to bond (Figs. 2(J–L)) the bottom layer of the microchip to a flat PMMA substrate containing the inlet and outlet reservoirs. To accomplish this, a second PMMA piece was trimmed to size, cleaned, and dried (Fig. 2(J)). Inlet and outlet reservoirs were drilled at appropriate locations (Fig. 2(K)). The surfaces of both PMMA substrates were treated with oxygen plasma at 20 W and 100 mTorr for 90 s in a plasma chamber (Plasma Etcher PE200, South Bay Technology, San Clemente, CA). Immediately following plasma treatment, both surfaces were silanized using a 10% tetraethyl orthosilicate (TEOS ≥ 99.0%) solution in 60:40 v/v isopropanol:water solution at 50°C for 30 min. Both PMMA substrates were treated again with oxygen plasma under the same conditions as described above. The two surfaces were brought into contact with proper alignment and pressed together with a hot press for 20 min at 75°C and 300 psi to form the desired microchip (Fig. 2(L)). Finally, the bonded chip went through a post-annealing bake for 2 h at 60°C to increase bonding strength.

2.4 Cascade microchip

A schematic representation of the cascade microchip is shown in Fig. 1. Initially, the microfluidic chip was filled completely with LE from the anode reservoir to the cathode reservoir using a 3 mL syringe. Next, PE and GFP, spiked into LE, were injected into the sample reservoir and filled through the T-channel toward the cathode reservoir so that LE occupying the region between the sample reservoir and cathode reservoir was flushed out of the cathode reservoir. In addition, only sample occupied the portion of the microchip between the sample reservoir and the cathode reservoir. This allows us to control the total mass load of sample (M_i). The cathode reservoir was rinsed several times with TE and then filled with TE. To avoid sample removal due to Laplace pressure differences between the sample reservoir and the cathode reservoir, vinyl electrical tape (Tartan™ 1710 Part No. 49656, USA) was placed over the sample reservoir prior to rinsing and filling the cathode reservoir with TE.

2.5 Experimental setup – fluorescent microscope and power supply

The loaded cascade microchip was mounted underneath the 4× objective lens of a Leica DMLB fluorescence microscope equipped with a CCD camera (SPOT RTcolor, Diagnostic Instruments, Sterling Heights, MI, USA). We controlled the camera using the software SPOT Advanced Version 3.5.9 (Diagnostic Instruments) to take individual photographs of the fluorescent proteins as they migrate through the microchannel via ITP. GFP and PE were excited with a mercury lamp (OSRAM HBO® 103W/2) using a filter cube (DMLB 513804, Leica Microsystems, IL, USA). Platinum electrodes were immersed in the cathode reservoir and anode reservoir, respectively. Initially, a voltage of 400 V was applied to the anode reservoir while the cathode reservoir was set to ground with an XHR 600-1 power supply (Xantrex Technology, Vancouver, Canada). As the proteins migrated toward the first reducing portion of the microchannel the voltage on the anode reservoir was reduced to 100 V so that the fluorescent proteins could be visually captured by the CCD camera. Without voltage reduction, the proteins migrate too fast for image capture due to the much higher current densities in the narrower regions of the microchannel. Images were collected with the SPOT advanced Version 3.5.9 software and modified using the crop function and the brightness/contrast function in Adobe Photoshop 5.5 (Adobe Systems, San Jose, CA) to remove background signal. Images were then transferred to ImageJ (http://rsb.info.nih.gov/ij) where electropherograms were obtained by plotting pixel number versus average intensity over the entire width of the channel.

3 Results and discussion

3.1 Theory – Nernst–Planck equation

The 3-D microchip includes two 10× reductions in cross-sectional area. A numerical simulation was developed using the Nernst–Planck-based transport equation, which describes the transport of ions subject to an electric field. The Nernst–Planck equation application mode is built directly into COMSOL Multiphysics v4.0a (COMSOL, Palo Alto, CA, USA) and is used in this paper to simulate all ion transport and protein migration through the microchip. The Nernst–Planck equation includes a transient term, a diffusive term, an electrophoretic term, a convective term, and a reaction term. The authors ignored electroosmotic flow and did not introduce any other flow to the system so that the Nernst–Planck equation reduces to

$$\frac{\partial c_i}{\partial t} + \nabla \cdot (-D_i \nabla c_i - z_i u_{m,i} F c_i \nabla \psi) = R_i \quad (3)$$

Table 1. Simulation parameters including electrophoretic mobilities (μ_i), diffusion coefficients (D_i), absolute mobilities (u_i), charges (z_i), and initial concentrations (c_i^0) for all ions solved in simulation

Species	$\mu_i \times 10^{-8}$ (m^2/(V s))	$D_i \times 10^{-9}$ (m^2/s)	$u_i \times 10^{-13}$ (s mol/kg)	z_i	c_i^0(mM)
Cl^-	−7.91	2.03	8.20	−1	$20,\ x \geq 0.0002$
H_3O^+	36.25	9.31	37.57	1	$10^{-pH_{LE}} \cdot 1000, x \geq 0.0002 + 10^{-pH_{TE}} \cdot 1000, x < 0.0002$
OH^-	−20.55	5.28	21.30	−1	$10^{-pOH_{LE}} \cdot 1000, x \geq 0.0002 + 10^{-pOH_{TE}} \cdot 1000, x < 0.0002$
$EACA^-$	−3.10	0.80	3.21	−1	$60 - c_{EACA^0}, x \leq 0.0002$
$EACA^0$	0	0.80	0	0	$\frac{60 c_{H_3O^+}}{[c_{H_3O^+} + K_{TE}]}, x \leq 0.0002$
$Ethanolamine^+$	4.43	1.14	4.59	1	$\sum_i z_i c_i = 0$
$Ethanolamine^0$	0	1.14	0	0	$\frac{K_{Ethanolamine} c_{Ethanolamine^+}}{c_{H_3O^+}}$
$Protein\_1^{10-}$	−4.00	0.20	0.83	−5	$2.5 \times 10^{-4}, 0.0002 \leq x \leq 0.0082$
$Protein\_2^{10-}$	−3.00	0.13	0.52	−6	$2.5 \times 10^{-4}, 0.0002 \leq x \leq 0.0082$

Note: $pH_{LE} = 9.5$ and $pH_{TE} = 10.0$.

where c_i is the concentration of species i, D_i is the diffusion coefficient of species i, z_i is the charge of species i, $u_{m,i}$ is the absolute mobility of species i, F is Faraday's constant (96485 C/mol), ψ is the electric potential, and R_i is the rate of production of species i. The electroneutrality condition [49] is also imposed so that

$$\sum_i z_i c_i = 0 \tag{4}$$

The positively charged ethanolamine component was the species the simulation used to ensure electroneutrality in the simulation and to satisfy Eq. (4). The electrophoretic mobilities (μ_i) of each ion were obtained from various sources [29, 30] and were related to the diffusion coefficient using the following relationship:

$$D_i = \frac{\mu_i \cdot R \cdot T}{z_i \cdot F} \tag{5}$$

where R is the universal gas constant (8.3145 J/(mol K)) and T is the temperature, taken to be 298.15 K. The absolute mobility was approximated using the Nernst–Einstein relation [49] which is only valid at low salt concentrations where:

$$u_{m,i} = \frac{D_i}{R \cdot T} \tag{6}$$

Electrophoretic mobilities, diffusion coefficients, absolute mobilities, charge, and initial ion concentrations in both the leading and TE are summarized in Table 1. Equations (3) and (4) are directly solved using COMSOL Multiphysics to observe the transient behavior and concentration distribution for all ions in the simulation.

3.2 Ionic reactions

To accurately model ITP in a microchannel, buffering reactions must be considered to account for the association of ions that may affect their effective mobility. The pH of the LE was 9.5 and the pH of the TE was 10.0 so that only the following ionic reactions need to be accounted for:

Table 2. Forward and reverse rate constants used in simulation

Rate constants	Value
$k_{f,EACA}$	10^6 mM/s
$k_{r,EACA}$	$5.62 \times 10^{13}\ s^{-1}$
$k_{f,Ethanolamine}$	10^6 mM/s
$k_{r,Ethanolamine}$	$3.16 \times 10^{12}\ s^{-1}$
$k_{f,Water}$	10^6 mM^2/s
$k_{r,Water}$	$10^{14}\ s^{-1}$

$$EACA^0 + H_2O \rightleftharpoons EACA^- + H_3O^+, \quad pK_{EACA} = 10.75 \tag{7}$$

$$Ethanolamine^+ + H_2O \rightleftharpoons Ethanolamine^0 + H_3O^+, \quad pK_{Ethanolamine} = 9.50 \tag{8}$$

$$2H_2O \rightleftharpoons OH^- + H_3O^+ \tag{9}$$

Other reactions that took place at low pH values, for instance the positively charged EACA species with $pK_a = 4.43$, are ignored because there were only trace amounts of this species present. The equilibrium expressions for ion concentrations used in the simulation have been developed as follows:

$$\frac{c_{EACA^-} \cdot c_{H_3O^+}}{c_{EACA^0}} = K_{EACA} = \frac{k_{f,EACA}}{k_{r,EACA}} = 1.78 \times 10^{-8}\ mM \tag{10}$$

$$\frac{c_{Ethanolamine^0} \cdot c_{H_3O^+}}{c_{Ethanolamine^-}} = K_{Ethanolamine} = \frac{k_{f,Ethanolamine}}{k_{r,Ethanolamine}} = 3.16 \times 10^{-7}\ mM \tag{11}$$

$$c_{H_3O^+} \cdot c_{OH^-} = K_W = \frac{k_{f,Water}}{k_{r,Water}} = 10^{-8}\ mM^2 \tag{12}$$

Kinetic rates are much faster than the characteristic mass transport [33, 34] and, as a result, fast forward and

reverse rate constants were specified to solve Eqs. (3) and (4) using the equilibrium relationships in Eqs. (10–12). Forward and reverse rate constants were specified so that all ions in the simulations were determined to be in chemical equilibrium. Forward and reverse rate constants ($k_{f,i}$, $k_{r,i}$) used in the simulation are summarized in Table 2.

The 3-D simulation was first drawn in COMSOL Multiphysics in a 2-D geometry and then extruded to three dimensions. The final geometry, which accounts for a single $10\times$ reduction in depth and a single $10\times$ reduction in width is shown in Fig. 3. In addition, only half of the actual microchannel was simulated because of symmetry in the *y*-direction and the simulation does discard the T-junction that is included in the experimental protocol to limit computational requirements. Neglecting the T-junction may introduce a small error in the concentration calculations as some sample will be lost when the protein migrates past the T-junction [16, 50], but the authors do not expect this loss to be more than 10% of the total mass.

The initial concentration distributions of all the ions and a potential profile need to be given to solve the simulation. The initial concentrations are summarized in Table 1. All the boundaries, labeled B1–B17 in Fig. 3 and their related boundary conditions are summarized in Table 3. B1 is the negatively charged cathode and B17 is the positively charged anode. The simulated proteins are negatively charged and migrate toward the anode.

3.3 Simulation results

The simulation includes the chloride ion, the hydronium, and hydroxide ions, the EACA ions (two charge states), the ethanolamine ions (two charge states), and two generic proteins (one charge state each). Chloride ion served as the leading ion in both the experiment and the simulation because it has a higher electrophoretic mobility than the proteins and most other anions [29]. EACA ion served as the trailing ion because it has a lower effective mobility than the proteins due to only being partially charged at pH 10.0 [16].

The authors were not able to include the protein reactions that influence protein valence and mobility as a result of changes in pH and ionic strength in the numerical simulations due to limitation on computer memory. Including pH dependence on the proteins net charge would have added an additional unknown for each charge state and exhausted the physical memory of the computer at a relatively low mesh density. However, the authors have performed 1-D ITP simulations on a cationic ITP system near pH 8 where inclusion of a protein titration curve did not significantly alter the final protein concentration profiles (data not shown). For these reasons, a single charge state was assigned to each protein. For additional information on how to include multiple charges states by the use of titration curves in 1-D ITP simulations see the work performed by Mosher et al. [51, 52].

The proteins migrated between the chloride ion and EACA ion in order of electrophoretic mobility. As the proteins migrate through the reducing unions, their concentrations should increase proportionally to the decrease in cross-sectional area until each protein reaches its maximum allowable concentration, i.e. the plateau concentration (Eq. 2), after which the peak width increases proportionally to the decrease in cross-sectional area. Initially, protein migration is slow due to the low current density in the large cross-sectional area portion of the channel; however, as the proteins migrate through the reducing unions, the zones migrate faster. The simulation results are shown in Figs. 4 and 5.

In Fig. 4, a series of cross-plots along the center of the channel and their corresponding surface plot are shown at various time points. The cross-plots were developed by drawing a line along the *x*-axis from cathode to anode and observing the concentration at different time points. In Fig. 4(A), the initial protein distribution in the microchannel geometry is shown for the generic protein 1 that has a higher electrophoretic mobility than generic protein 2. Both proteins have an initial concentration of 0.25 μM and initially occupy a length of 8 mm. The cross-sectional geometry is half of the actual experimental microchip because of symmetry in the *y*-direction. Therefore, the cross-sectional area of the simulated microchannel is 100 μm × 500 μm (depth × width). In Fig. 4(B), the protein is beginning to concentrate at the TE interface, but has only concentrated by a factor of two after 100 s of the run time. In Fig. 4(C), the protein band is approaching the first reducing union and has concentrated by a factor of ∼20 after 500 s. At this point, there is a slight distortion and frontal tailing as the protein approaches the first reducing union. In Fig. 4(D), the protein band has passed the first reducing union and corrected any distortion that had previously occurred. In addition, the *x*-axis has been modified so that the peak attributes can be visualized. It is clear that the protein is still running in peak mode as opposed to plateau mode. Therefore, the protein has yet to reach its maximum

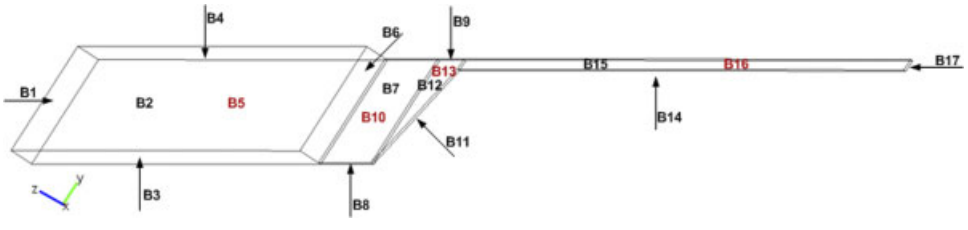

Figure 3. Schematic of 3-D domain solved using COMSOL v4.0a. The domain includes a straight microchannel 3.2 cm long with one depth change and one width change at 1 cm and 1.3 cm from the cathode (B1), respectively. B1-B17 represents the boundaries

or plateau concentration as defined by Eq. (2). In Fig. 4(E), the protein band has formed a tight band and is beginning to pass through the second reducing union. There is very little additional concentration between Figs. 4(D) and (E). However, at 623.5 s (Fig. 4(F)) the protein band has migrated into the narrowest portion of the microchannel and has concentrated considerably to ~2.85 mM, which is less than 4% from the calculated plateau concentration using Eq. (2) (see discussion below). Therefore, the protein has concentrated from 0.25 μM to 2.85 mM a concentration factor of approximately 11 400.

Table 3. Boundary conditions from Fig. 3 used for Nernst–Planck application modes (COMSOL Multiphysics v4.0a)

Boundary	c_i (mM)	ψ (V)
B1	c_i^0	0
B2–B16	Insulation/symmetry	Insulation/symmetry
B17	c_i^0	400

The final concentration distributions of all the anions in the system including the LE, two generic proteins, and TE are revealed in Fig. 5. The components have formed relatively pure zones in order of effective electrophoretic mobility. Both the leading and TE concentrations were divided by a factor of 10 to visualize all anions on the same scale. The final concentration for generic protein 2 was

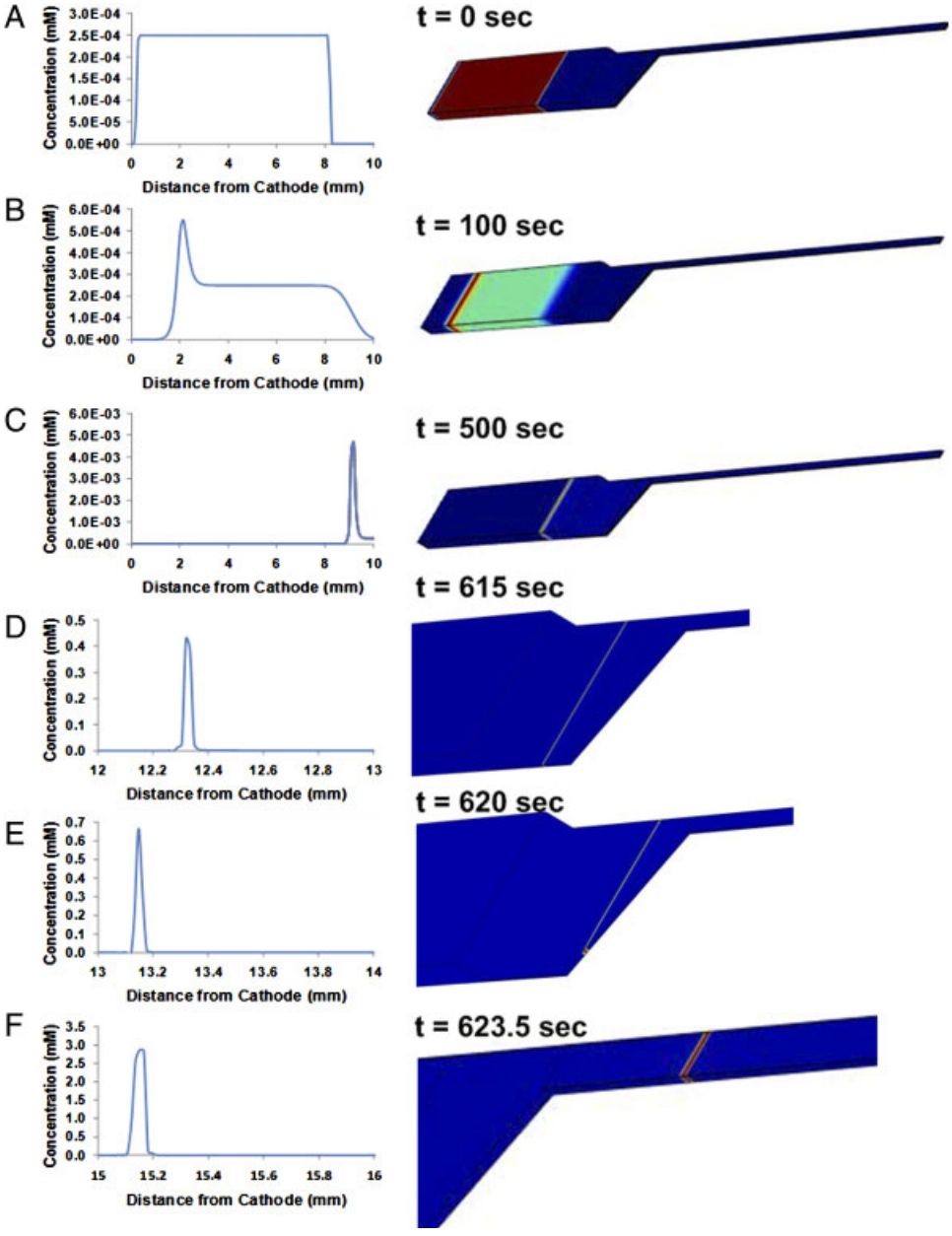

Figure 4. A series of cross-plots along the center of the channel and their corresponding surface plot are shown at various time points during ITP. (A) The initial protein concentration, 0.25 μM, and its distribution in the channel. (B) At 100 sec, the protein begins to concentrate at the terminator interface. (C) The protein, which has nearly reached its steady-state, peak-mode concentration in the first section of the channel approaches the 1st reducing union at 500 sec. (D) The protein has migrated through the first reducing union and has reached a peak concentration of ~0.4 mM. (E) As it approaches the second reducing union, the protein has formed a tight peak close to its steady-state, peak-mode concentration at this current density. (F) At 623.5 sec, the protein has migrated into the narrowest portion of the microchannel and has nearly reached its steady-state plateau-mode concentration, ~2.85 mM, having undergone a net concentration factor of 11400 from start to finish.

approximately 2.05 mM, a concentration increase of 8200. Typically, in simulations of ITP, protein concentrations do not exceed 1 mM [51–54]; however, these concentrations are highly dependent on the protein charge state, as can be seen from Eq. (2). For instance, when the simulation parameters (Table 1) are plugged into Eq. (2), the resulting concentrations for the generic proteins are ~2.96 and 2.10 mM, respectively. These relatively high concentrations are attributed to the low charge, −5 and −6, assigned to the proteins here. However, when charge states of −20 and −30 are used to calculate the plateau concentration from Eq. (2) for generic protein 1, the results are 0.74 and 0.42 mM. Thus, the final concentrations are highly dependent on the charge state. In any case, the concentrations obtained from the simulation are within 4% of the calculated plateau concentrations from Eq. (2).

Moment analysis, modified from temporal to spatial moments [55, 56], was also performed using the simulation software to calculate protein attributes such as the variance (σ^2) and peak width and is described below. Briefly, the n^{th} moment (m_n) is given by

$$m_n = \int_a^b c(x) \cdot x^n \, dx \tag{13}$$

where $c(x)$ is the intensity value of the concentration of the protein, x is the spatial position, and a and b are truncated integration limits around the peaks in the simulation. The truncated values occurred at distances of 1.45 and 1.60 cm from the cathode. The variance is then calculated from the following relationship [56]:

$$\sigma^2 = \frac{m_2}{m_0} - \left(\frac{m_1}{m_0}\right)^2 \tag{14}$$

and the subsequent peak width (w_i) for each peak is given by

$$w_i = 4\sigma \tag{15}$$

A comparison of peak widths, final protein concentrations, and concentration factors for the two simulated proteins are shown in Table 4.

The pH profile based on both the hydronium (pH) and hydroxide (pH_2) concentrations was compared to ensure that equilibrium was established in the simulation and were defined as

$$\text{pH} = -\log_{10}(\text{H}^+/1000) \tag{16}$$

$$\text{pH}_2 = 14 + \log_{10}(\text{OH}^-/1000) \tag{17}$$

There is strong agreement between the hydronium-based pH and the hydroxide-based pH ensuring that equilibrium for all the buffering ions has been established (Fig. 5). Simulation results indicate a pH excursion of approximately 1 pH unit from the LE to TE. However, the pH through the protein zones is incorrect because protein titration curves that take into account the protein charge were not included in the simulation. The overall pH profile, except at positions where the proteins was located, looks consistent with previous results that included the proteins titration curve [51, 52]. In addition, the authors are only including the pH profile to demonstrate that equilibrium between the reactant ions has been established. The authors used forward and reverse rate constants (Table 2) that were high enough ($k_{f,i} = 10^6$) to ensure equilibrium of all the buffering ions in the system throughout the simulation. Typically, simulations in the literature use infinitely fast kinetics with hydronium as the electroneutral species, but this approach demonstrates that fast kinetics can also be applied.

3.4 Experimental results

In order to evaluate simulation performance, ITP was performed on two fluorescent proteins, PE and GFP, in a cascade microfluidic chip representative of the model. The experimental microchannel is shown in Fig. 1 and includes a 100 × reduction in cross-sectional area from inlet to outlet, a T-channel to control sample loading, and cathode, sample, and anode reservoirs, respectively. The proteins were both negatively charged at the running pH and migrated from cathode to anode when power was applied.

Initially, the protein migration was slow due to the low current density in the large cross-sectional area portion of the channel. However, as the proteins approached the first reducing union, they began to migrate too fast for the CCD camera to capture representative images. The CCD camera required an integration time of ~1 s to collect photographs of what was occurring in the microchip and, as a result, at the current voltage setting camera artifacts transpired. Consequently, the voltage was decreased from 400 to 100 V as the proteins approached the first reducing union, which decreased the velocity of the moving proteins and allowed the camera to capture photographs that produced an accurate representation of what was happening in the microchip and what was visualized in real-time by the microscope.

Representative pictures of the ITP migration at various positions in the microfluidic chip are illustrated in Fig. 6. Figure 6(A) represents the protein starting to stack out and gain enough mass to be visualized by the camera. As the protein passes the T-junction there is a slight distortion that occurs and some mass is lost into the side channel (Fig. 6(B)). The proteins then migrate past the first reduction where an increase in signal is observed (Fig. 6(C)). Next, the proteins migrate past the second reduction where slight distortion and separation of the protein bands occur (Fig. 6(D)). The distortion is normal as proteins migrate through a reduction in the cross-sectional area [26, 27]; however, with sufficient migration length from the reduction to the detection point the ITP bands self-correct. This phenomenon is observed in Fig. 6(E) where the proteins have migrated a sufficient distance into the small cross-sectional area section of the channel and formed distinct zones with no separation between the protein bands.

Table 4. Summary of simulated and experimental peak widths (w_i) determined from moment analysis, final concentrations (c_i), and concentration factors (CF_i) for two simulated proteins, and for experimental proteins, PE and GFP

Simulation	Protein 1			Protein 2		
	w_1 (μm)	c_1 (mM)	CF_1	w_2 (μm)	c_2 (mM)	CF_2
	115.4	2.85	11 400	124.7	12.05	8200

Experimental	PE				GFP			
Trial #	w_{PE} (μm)	c_{PE} (mg/mL)	c_{PE} (mM)	CF_{PE}	w_{GFP} (μm)	c_{GFP} (mg/mL)	c_{GFP} (mM)	CF_{GFP}
1	46.67	34.20	0.14	17 142	69.57	22.94	0.85	11 499
2	56.17	28.41	0.12	14 243	87.99	18.14	0.67	9092
3	45.48	35.09	0.15	17 590	58.34	27.36	1.01	13 713
Average	49.44	32.57	0.14	16 325	71.97	22.81	0.84	11 435
St. dev.	5.86	3.63	0.02	1817	14.97	4.61	0.17	2311

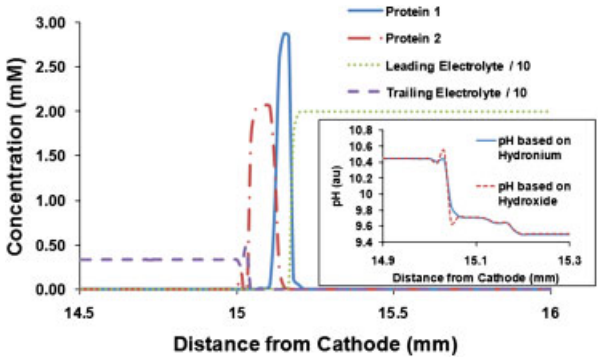

Figure 5. Final concentration distribution from simulation of relevant anions. The two generic proteins have concentrated and formed nearly pure zones between the leading electrolyte and trailing electrolyte. The concentrations for the two proteins are approximately 2.85 and 2.05 mM. Both the leading and trailing electrolyte concentrations have been divided by a factor of 10 in order to see all the anionic components on the same plot. The inset shows the pH profile based on both the hydronium and hydroxide species indicating equilibrium has been established in the simulation. In addition, the pH changes from pH 9.5 at the leading electrolyte to approximately pH 10.5 in the trailing electrolyte due to the chemical equilibrium established in the microchannel

The authors do not completely understand why the separation between bands occurs. Three plausible hypotheses are that (i) a small amount of the TE migrates in front of the second protein because of the distortion and eventually self-corrects, (ii) chloride ion from the sample reservoir and T-channel diffuse into the channel and forms a band that eventually catches up to the LE but has to migrate past the two proteins which results in a temporary gap between the two proteins, or (iii) hydroxide ion migrating in the opposite direction of ITP passes through the protein bands and causes a temporary gap. The authors do not believe that carbon dioxide effects that are detrimental to ITP experiments [44] are occurring here because solutions are degassed prior to ITP experiments and, also, the gap does not persist throughout the experiment.

A representative picture of the two protein bands stacked and concentrated in the small-cross-sectional area portion of the channel is observed in Fig. 6(E). The entire ITP migration from cathode to anode is completed in less than 20 min. For a complete visualization of the protein migration through the microfluidic-tapered channel, see the ITP video provided in the Supporting Information. Three successive trials of ITP in the tapered microfluidic chip at the end of the experiment are shown in Fig. 7. The experiments were repeated three times to show reproducibility and develop statistical information. Electropherograms for each protein were collected from Fig. 7 and moment analysis was performed as previously described to obtain protein attributes such as peak widths (w_i) for both proteins. The integration limits from Eq. (13) were based on the field of view of the camera shown in Fig. 7 and the moments were calculated using the trapezoidal rule [57] with discrete position values such that

$$m_n = \frac{\int_i (x_{i+1} - x_i)(c(x_{i+1}) \cdot x_{i+1}^n + c(x_i) \cdot x_i^n)}{2} \quad (18)$$

The variances and peak widths are calculated as previously described. The peak widths for PE and GFP were 49.44 ± 5.86 and 71.97 ± 14.97 μm, respectively and are shown in Table 4. In order to calculate the final experimental concentrations, the initial mass load of each protein was required.

The initial mass loads of the proteins were controlled experimentally by incorporating a T-channel into the microfluidic chip. Proteins were loaded from the sample reservoir to the cathode reservoir so that protein solution occupied only the sample-loading zone (Fig. 1). The initial mass load was calculated by rearranging Eq. (1) to solve for M_i where all other parameters in Eq. (1) are known including the cross-sectional area (0.1 mm^2), the initial protein concentration (1.995 μg/mL), and the length of the sample-loading zone (8 mm). The initial mass load for both proteins was approximately 1.6 ng, which is equivalent to 6.67 fmol for PE and 59.3 fmol for GFP,

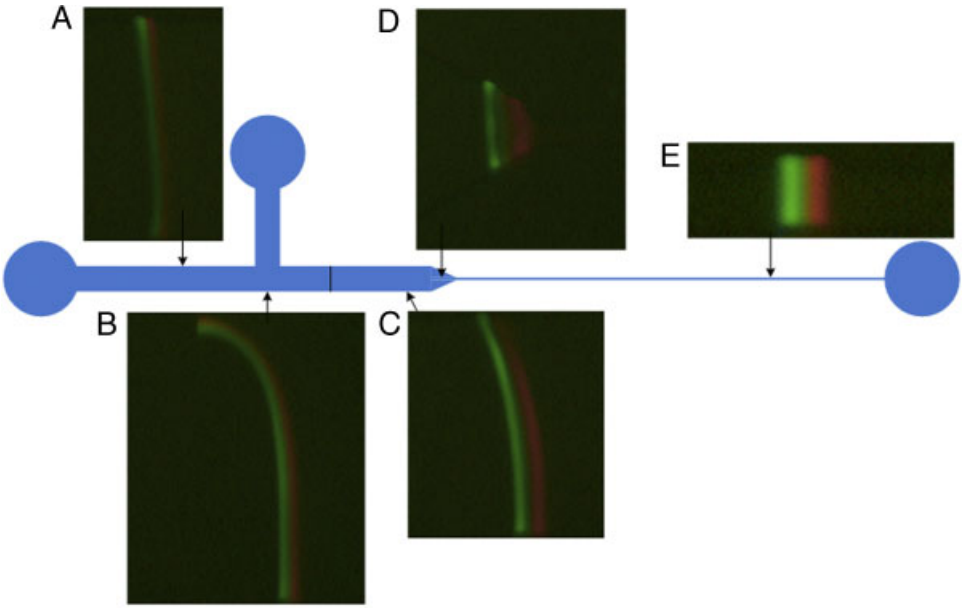

Figure 6. Experimental ITP stacking of PE and GFP at different sections of the microchannel. (A) The proteins are beginning to stack but are difficult to visualize. (B) The proteins have collected most of the total mass and are migrating through the T-junction where some sample is lost. (C) The proteins have passed the first junction where the depth change occurs and are now clearly visible. Some separation between the proteins is observed. (D) The proteins are going through the width change and again some separation between protein bands is observed. (E) The proteins are in the small cross-sectional area portion of the channel and all the distortions including the gaps between protein bands seen previously have now been eliminated due to ITP's self-sharpening effect. The proteins have stacked and concentrated into nearly pure zones.

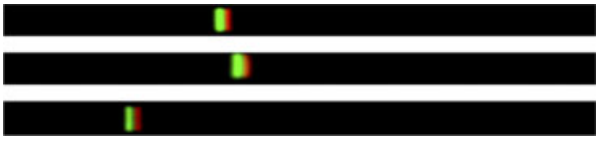

Figure 7. Experimental results of two fluorescent proteins for three subsequent trials near the end of the ITP experiment. PE (red) migrates in front of the GFP (green) because it has a higher electrophoretic mobility at the running pH. The images have been cropped and modified to subtract out background noise using Adobe Photoshop 5.5

respectively. The final protein concentrations were calculated from Eq. (1) using the peak widths obtained from moment analysis, the initial mass loads (1.6 ng), and the cross-sectional area of the narrow region of the microchannel (0.001 m^2).

The final concentrations for PE and GFP were calculated to be 32.57 ± 3.63 mg/mL (0.14 ± 0.02 mM) and 22.81 ± 4.61 mg/mL (0.84 ± 0.17 mM), respectively. The concentration factor is found by dividing the final protein concentration by the initial protein concentration. This yielded concentration factors for PE and GFP of $16\,325 \pm 1817$ and $11\,435 \pm 2311$, respectively. The final concentrations and concentrations factors for each trial along with the corresponding average values and standard deviation for both PE and GFP are shown in Table 4.

It is not surprising that the relative error between runs was high (~10% for PE and ~20% for GFP) since the experimental system was not automated. Reproducibility problems could be mitigated by automating the system; however, the authors did not take any steps to write a computer code to automate the experiment. In addition, the authors did not see any sample adsorption to the channel walls, even after repeated experiments, confirming that the final protein bands consisted of all the protein loaded on to the microchip. This was further confirmed by running ghost experiments where the sample consisted only of LE and the ITP was performed in the usual manner. No protein bands were observed in this case.

In conclusion, these results indicate that we observe a $100\times$ increase in concentration due to the reduction in cross-sectional area and a greater than $100\times$ increase in concentration due to the ITP stacking effect. Thus, the total concentration factor of both PE and GFP exceeds 10 000.

4 Concluding remarks

This paper describes the concentration of proteins by ITP in a cascade microfluidic chip and the development of a 3-D numerical simulation. The numerical 3-D simulation provided a convenient tool to analyze protein migration through the cascade microchannel. The simulated microchannel includes two $10\times$ reductions in cross-sectional area to demonstrate protein concentration as the proteins migrate into narrower regions of the microchannel. The

proteins stacked out into pure zones between the leading and trailing ions according to their electrophoretic mobilities. Fast kinetics, rather than infinite kinetics were used in the simulation to account for buffering reactions, and the association of ions that may affect their effective mobilities. The forward reaction rates were chosen so that equilibrium between all buffering ions was achieved. In addition, the simulation demonstrated that two generic proteins could be concentrated by factors of 11 400 and 8200, respectively. This is the first 3-D simulation of ITP and opens up the door to simulating ITP and other electrophoretic techniques in complex geometries. The ITP simulation in the cascade microchip was also compared to experimental results.

ITP of two fluorescent proteins, PE and GFP, was performed in a PMMA microfluidic chip whose geometry was consistent with the simulated microchannel. The proteins were introduced into the microchip through a T-channel to control the sample load. PE and GFP were both negatively charged at the system pH (the pH of LE was 9.5 and the pH of TE was 10.0) and migrated toward the anode. The two proteins formed two adjacent zones between the LE and TE. The concentration and resulting fluorescent signal became brighter as the protein bands migrated through the microchip into smaller cross-sectional area sections of the channel. The entire experiment could be completed in less than 20 min with applied voltages ranging from 400 to 100 V. Both proteins increased their concentrations by more than a factor of 10 000 which is in agreement with the concentration factor predicted by the simulation. This is the highest published concentration factor of proteins using only ITP. In addition, the experimental results agreed qualitatively with simulation predictions.

The research was supported by the Life Science Discovery Fund and the Washington State University National Institutes of Health Protein Biotechnology Training Program Award Number T32GM008336 from the NIGMS. The content is solely the responsibility of the authors and does not necessarily represent the official views of the National Institute of General Medical Sciences or the National Institutes of Health.

The authors have declared no conflict of interest.

5 References

[1] Hatch, A. V., Herr, A. E., Throckmorton, D. J., Brennan, J. S., Singh, A. K., *Anal. Chem.* 2006, *78*, 4976–4984.

[2] Yu, C. J., Tseng, W. L., *Electrophoresis* 2006, *27*, 3569–3577.

[3] Foote, R. S., Khandurina, J., Jacobson, S. C., Ramsey, J. M., *Anal. Chem.* 2005, *77*, 57–63.

[4] Herr, A. E., Hatch, A. V., Throckmorton, D. J., Tran, H. M., Brennan, J. S., Giannobile, W. V., Singh, A. K., *Proc. Natl. Acad. Sci. USA* 2007, *104*, 5268–5273.

[5] Kelly, R. T., Li, Y., Woolley, A. T., *Anal. Chem.* 2006, *78*, 2565–2570.

[6] Kutter, J. P., Jacobson, S. C., Ramsey, J. M., *J. Microcolumn Sep.* 2000, *12*, 93–97.

[7] Jemere, A. B., Martinez, D., Finot, M., Harrison, D. J., *Electrophoresis* 2009, *30*, 4237–4244.

[8] Yang, W. C., Sun, X. H., Pan, T., Woolley, A. T., *Electrophoresis* 2008, *29*, 3429–3435.

[9] Yu, C., Davey, M. H., Svec, F., Frechet, J. M. J., *Anal. Chem.* 2001, *73*, 5088–5096.

[10] Jacobson, S. C., Ramsey, J. M., *Electrophoresis* 1995, *16*, 481–486.

[11] Kutter, J. P., Ramsey, R. S., Jacobson, S. C., Ramsey, J. M., *J. Microcolumn Sep.* 1998, *10*, 313–319.

[12] Jung, B., Bharadwaj, R., Santiago, J. G., *Electrophoresis* 2003, *24*, 3476–3483.

[13] Mohamadi, M. R., Kaji, N., Tokeshi, M., Baba, Y., *Anal. Chem.* 2007, *79*, 3667–3672.

[14] Li, Y., DeVoe, D. L., Lee, C. S., *Electrophoresis* 2003, *24*, 193–199.

[15] Breadmore, M. C., Quirino, J. P., *Anal. Chem.* 2008, *80*, 6373–6381.

[16] Cui, H. C., Dutta, P., Ivory, C. F., *Electrophoresis* 2007, *28*, 1138–1145.

[17] Jung, B., Bharadwaj, R., Santiago, J. G., *Anal. Chem.* 2006, *78*, 2319–2327.

[18] Jung, B. G., Zhu, Y. G., Santiago, J. G., *Anal. Chem.* 2007, *79*, 345–349.

[19] Wang, J., Zhang, Y., Mohamadi, M. R., Kaji, N., Tokeshi, M., Baba, Y., *Electrophoresis* 2009, *30*, 3250–3256.

[20] Gebauer, P., Mala, Z., Boček, P., *Electrophoresis* 2009, *30*, 29–35.

[21] Wainright, A., Williams, S. J., Ciambrone, G., Xue, Q. F., Wei, J., Harris, D., *J. Chromatogr. A* 2002, *979*, 69–80.

[22] Everaerts, F. M., Routs, R. J., *J. Chromatogr. A* 1971, *58*, 181–194.

[23] Bier, M., Cuddeback, R. M., Kopwillem, A., *J. Chromatogr. A* 1977, *132*, 437–450.

[24] Baumann, G., Chrambach, A., *Proc. Natl. Acad. Sci. USA* 1976, *73*, 732–736.

[25] Kopwillem, A., Merriman, W. G., Cuddeback, R. M., Smolka, A. J., Bier, M., *J Chromatogr.* 1976, *118*, 34–46.

[26] Dolnik, V., Deml, M., Boček, P., *J. Chromatogr.* 1985, *320*, 89–97.

[27] Slais, K., *Electrophoresis* 1995, *16*, 2060–2068.

[28] Everaerts, F. M., Mikkers, F. E. P., Verheggen, T. P. E. M., *Analytical Isotachophoresis: Proceedings of the 2nd International Symposium on Isotachophoresis, Eindhoven, September 9– 11, 1980*, Elsevier, New York 1981.

[29] Mosher, R. A., Saville, D. A., Thormann, W., *The Dynamics of Electrophoresis*, VCH, Weinheim, New York 1992.

[30] Boček, P., Deml, M., Gebauer, P., Dolnik, V., *Analytical Isotachophoresis*, VCH, Weinheim, Germany 1988.

[31] Bier, M., Palusinski, O. A., Mosher, R. A., Saville, D. A., *Science* 1983, *219*, 1281–1287.

[32] Thormann, W., Breadmore, M. C., Caslavska, J., Mosher, R. A., *Electrophoresis* 2010, *31*, 726–754.

[33] Palusinski, O. A., Graham, A., Mosher, R. A., Bier, M., Saville, D. A., *AIChE J.* 1986, *32*, 215–223.

[34] Saville, D. A., Palusinski, O. A., *AIChE J.* 1986, *32*, 207–214.

[35] Hruska, V., Jaros, M., Gas, B., *Electrophoresis* 2006, *27*, 984–991.

[36] Hruska, V., Gas, B., Vigh, G., *Electrophoresis* 2009, *30*, 433–443.

[37] Bercovici, M., Lele, S. K., Santiago, J. G., *J. Chromatogr. A* 2009, *1216*, 1008–1018.

[38] Bahga, S. S., Bercovici, M., Santiago, J. G., *Electrophoresis* 2010, *31*, 910–919.

[39] Shim, J., Dutta, P., Ivory, C. F., *Electrophoresis* 2007, *28*, 572–586.

[40] Shim, J., Dutta, P., Ivory, C. F., *Electrophoresis* 2009, *30*, 723–731.

[41] Chou, Y., Yang, R. J., *Electrophoresis* 2009, *30*, 819–830.

[42] Paschkewitz, J. S., Molho, J. I., Xu, H., Bharadwaj, R., Park, C. C., *Electrophoresis* 2007, *28*, 4561–4571.

[43] Kaneta, T., Ueda, T., Hata, K., Imasaka, T., *J. Chromatogr. A* 2006, *1106*, 52–55.

[44] Khurana, T. K., Santiago, J. G., *Lab Chip* 2009, *9*, 1377–1384.

[45] Stachowiak, T. B., Svec, F., Frechet, J. M., *J. Chromatogr. A* 2004, *1044*, 97–111.

[46] Bai, Y. L., Koh, C. G., Boreman, M., Juang, Y. J., Tang, I. C., Lee, L. J., Yang, S. T., *Langmuir* 2006, *22*, 9458–9467.

[47] Tennico, Y. H., Koesdjojo, M. T., Kondo, S., Mandrell, D. T., Remcho, V. T., *Sens. Actuators, B* 2010, *143*, 799–804.

[48] Cui, H. C., Horiuchi, K., Dutta, P., Ivory, C. F., *Anal. Chem. B* 2005, 77, 1303–1309.

[49] Newman, J. S., Thomas-Alyea, K. E., *Electrochemical Systems*, Wiley, Hoboken, NJ 2004.

[50] Cui, H. C., Huang, Z., Dutta, P., Ivory, C. F., *Anal. Chem.* 2007, *79*, 1456–1465.

[51] Mosher, R. A., Dewey, D., Thormann, W., Saville, D. A., Bier, M., *Anal. Chem.* 1989, *61*, 362–366.

[52] Mosher, R. A., Gebauer, P., Caslavska, J., Thormann, W., *Anal. Chem.* 1992, *64*, 2991–2997.

[53] Thormann, W., Firestone, M. A., Sloan, J. E., Long, T. D., Mosher, R. A., *Electrophoresis* 1990, *11*, 298–304.

[54] Thormann, W., Mosher, R. A., *Electrophoresis* 1990, *11*, 292–298.

[55] Abramowitz, M., Stegun, I. A., *Handbook of Mathematical Functions, with Formulas, Graphs, and Mathematical Tables*, Dover Publications, New York 1972.

[56] Levenspiel, O., *Chemical Reaction Engineering*, Wiley, New York 1972.

[57] Kreyszig, E., *Advanced Engineering Mathematics*, John Wiley, Hoboken, NJ 2006.

